Article

Patterns

Interpretable machine learning reveals hemispheric asymmetry of state switching in the suprachiasmatic nucleus

Graphical abstract

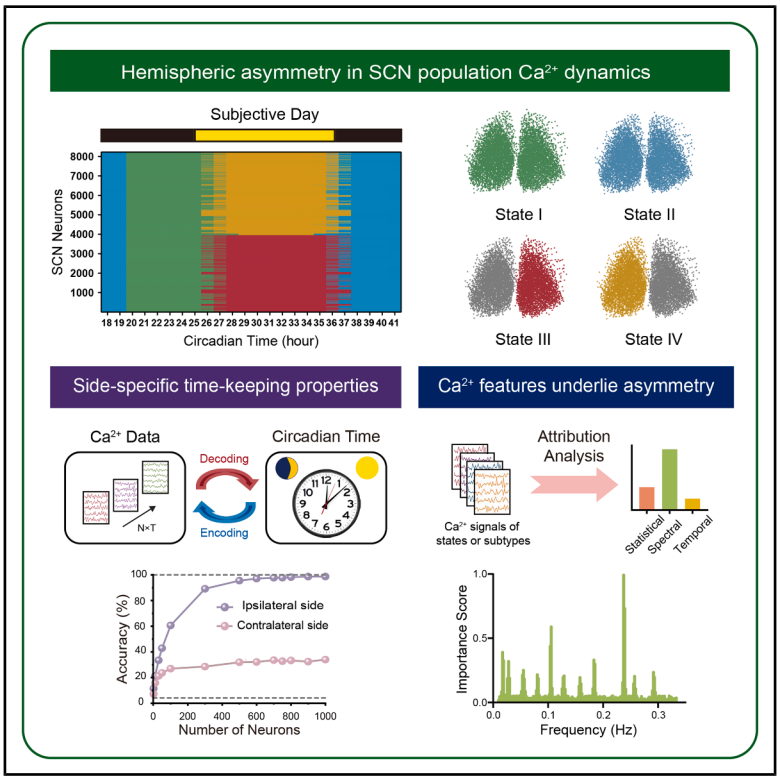

Highlights

- An interpretable ML framework for integrative analysis of SCN population Ca^{2+} signals
- ST states and neuron subtypes show hemispheric asymmetry during the subjective day
- Each SCN hemisphere encodes a full yet distinctive time feature representation
- Spectral features are major discriminative elements of hemispheric asymmetry

Authors

Zongpeng Zhang, Zichen Wang, Jing Yu, ..., Zhouchen Lin, Heping Cheng, Xiao-Hua Zhou

Correspondence

chengp@pku.edu.cn (H.C.), azhou@math.pku.edu.cn (X.-H.Z.)

In brief

Zhang et al. developed an interpretable machine learning framework to analyze population-level calcium ion signals in the suprachiasmatic nucleus (SCN), the central circadian clock of mammals. They uncover a hemispheric asymmetry in the SCN, particularly during the subjective day. Time prediction experiments further show that each hemisphere encodes differential time-encoding features. The work highlights hemispheric asymmetry as a fundamental property of the brain's circadian clock.

Zhang et al., 2026, Patterns 7, 101617
September 11, 2026
https://doi.org/10.1016/j.patter.2026.101617

CellPress

Please cite this article in press as: Zhang et al., Interpretable machine learning reveals hemispheric asymmetry of state switching in the suprachiasmatic nucleus, Patterns (2026), https://doi.org/10.1016/j.patter.2026.101617

Patterns

CellPress
OPEN ACCESS

Article

Interpretable machine learning reveals hemispheric asymmetry of state switching in the suprachiasmatic nucleus

Zongpeng Zhang,[1,11] Zichen Wang,[2,11] Jing Yu,[2,3] Mingqing Xiao,[4,5] Haoxuan Li,[6] Zongkun Zhang,[7] Xiheng Fang,[2] Ying Xu,[8] Lei Ma,[2] Zhouchen Lin,[4] Heping Cheng,[2,3,*] and Xiao-Hua Zhou[1,9,10,12,*]

[1]Department of Biostatistics, School of Public Health, Peking University, Beijing 100191, China
[2]National Biomedical Imaging Center, State Key Laboratory of Membrane Biology, Institute of Molecular Medicine, Peking-Tsinghua Center for Life Sciences, College of Future Technology, Peking University, Beijing 100871, China
[3]PKU-Nanjing Institute of Translational Medicine, Nanjing, Jiangsu 210032, China
[4]State Key Lab of General AI, School of Intelligence Science and Technology, Peking University, Beijing 100871, China
[5]Microsoft Research Asia, Singapore 069547, Singapore
[6]Institute for Artificial Intelligence, Peking University, Beijing 100871, China
[7]State Key Laboratory of Advanced Optical Communication Systems and Networks, School of Electronics, Peking University, Beijing 100871, China
[8]Biomedical Basic Research Center (BBRC) of Jiangsu, Soochow University, Suzhou, Jiangsu 215123, China
[9]Beijing International Center for Mathematical Research, Peking University, Beijing 100871, China
[10]Peking University Chongqing Research Institute of Big Data, Chongqing 401331, China
[11]These authors contributed equally
[12]Lead contact
*Correspondence: chengp@pku.edu.cn (H.C.), azhou@math.pku.edu.cn (X.-H.Z.)
https://doi.org/10.1016/j.patter.2026.101617

THE BIGGER PICTURE Timekeeping is one of the brain's fundamental functions. Mammals anticipate daily environmental changes through an internal clock located in the suprachiasmatic nucleus (SCN), a bilaterally symmetric brain nucleus comprising approximately 20,000 neurons. Accurate timekeeping therefore depends not only on individual cellular rhythms but also on how thousands of SCN neurons interact within and across both hemispheres to compute time.

In this study, we demonstrate that the left and right sides of the SCN do not tick in synchrony during the daytime, extending the broader principle of brain asymmetry to the central circadian clock. Our findings suggest that even a structurally symmetric brain system can display functional asymmetry to support stable timekeeping. In addition, this work shows how interpretable AI can help reveal design principles in complex neural systems.

SUMMARY

The suprachiasmatic nucleus (SCN) is the master circadian clock in mammals, comprising ~20,000 neurons organized into a bilaterally symmetric oval structure. System-level time computations in the SCN depend on coordinated spatiotemporal patterns of neuronal activity, yet most prevailing methods perform time-series analyses while disregarding neural spatiotemporal organization. Here, we developed an interpretable machine learning framework for the integrative analysis of large-scale spatiotemporal calcium signals from SCN neurons, with built-in validation and biological interpretability. Applying this framework, we identified distinct neural spatiotemporal states and subtypes whose spatial mapping across hemispheres revealed hemispheric asymmetry, particularly during the subjective day. Circadian timekeeping ability also displayed side specificity, with each hemisphere encoding a full yet unique time feature representation. Attribution analysis further indicated spectral features of calcium signals as the primary discriminative elements underlying this asymmetry. Overall, we demonstrate that hemispheric asymmetry of state switching is a fundamental property of the brain's circadian clock.

Please cite this article in press as: Zhang et al., Interpretable machine learning reveals hemispheric asymmetry of state switching in the suprachiasmatic nucleus, Patterns (2026), https://doi.org/10.1016/j.patter.2026.101617

INTRODUCTION

The suprachiasmatic nucleus (SCN), the central circadian clock of mammals, orchestrates daily physiological and behavioral rhythms through multichannel signaling from approximately 20,000 heterogeneous neurons.[1–3] This bilaterally symmetrical, oval-shaped structure, which is entrained to the 24-h light-dark (LD) cycle,[4] serves as a compelling model for exploring how complex neuronal interactions give rise to emergent activities at the cellular, network, and whole-system levels.[5] Within the SCN, calcium (Ca^{2+}) signals integrate information from neuronal network electrophysiology, paracrine communications, and intracellular pathways, including those driven by the circadian transcriptional-translational feedback loop.[6] These circadian Ca^{2+} rhythms exhibit spatiotemporally ordered sequential activation patterns across the SCN.[1,2,7–9] At the single-neuron level, SCN Ca^{2+} activities are highly heterogeneous and display multiscale dynamics in which individual Ca^{2+} bursts act as fundamental units that form higher-order temporal structures, such as Ca^{2+} states and modes.[10] Decoding these Ca^{2+} signals at the system level is therefore essential for elucidating the mechanisms underlying circadian timekeeping in the SCN.

Recent advances in high-throughput Ca^{2+} imaging and computational and mathematical tools for large-scale data analysis have provided unprecedented opportunities to explore SCN datasets and reveal system-level mechanisms and emergent properties.[1,10–16] In particular, machine learning has proven effective in analyzing intricate neural systems because of its ability to uncover hidden features and emergent patterns from large-scale data.[10,17,18] For example, clustering algorithms paired with neural networks[10] and other representation learning methods for time series[11,19,20] have been employed to identify distinct SCN cell types and functional subgroups. These new investigative tools have revealed the group-decision timekeeping mechanism of the SCN, i.e., random polling of approximately 900 neurons across these subgroups can predict hourly time with 99% precision.[10] These exciting advances offer a new paradigm for deciphering biological rules and principles from high-dimensional experimental data.

However, we are only at the beginning of developing a battery of machine learning tools and, with them, tapping the rich information concealed in large datasets on the SCN. In this context, previous studies failed to integrate prior spatial and temporal biological information,[1,11] precluding the exploration of functional properties and organization that require spatial and temporal interplay among SCN neurons. Furthermore, the "black-box" nature of machine learning methods complicates validation and interpretation within the context of SCN function.[21]

In this study, we developed an interpretable machine learning framework that integrates spatiotemporal priors to analyze SCN Ca^{2+} rhythms and assess time predictability using both a recently released dataset and a newly collected dataset (Figure 1). Our results revealed hemispheric asymmetry in SCN population Ca^{2+} dynamics, particularly during the subjective day. Furthermore, attribution analysis using an adversarially disentangled neural network (ADNN) identified spectral features of the Ca^{2+} signal as major discriminative elements associated with this asymmetry, alongside contributions from temporal and statistical features.

RESULTS

Overview of the proposed machine learning framework

To analyze the timekeeping properties of the SCN at the system level, we used two large-scale SCN Ca^{2+} imaging datasets with different acquisition strategies as inputs. The first was obtained from a recently reported dataset,[10] which consisted of six SCN slices (650 × 650 × 300 μm) from adult *Viaat-Cre::GCaMP6s* mice, with 5 min of volumetric Ca^{2+} imaging every hour over an entire circadian period. We refer to these as 3D-t slices. Each slice consisted of 6,000–9,000 segmented neurons, and a total of 45,301 SCN neurons were recorded at a rate of 0.61–0.67 Hz. The other dataset consisted of continuous single-plane recordings (frame rate of 2.67–2.72 Hz) from a total of 426 SCN neurons over 3–4 h in three slices obtained from adult *Viaat-Cre::GCaMP6f* mice, and these recordings are referred to as 2D-t slices. These high-dimensional, multiscale-sampled datasets should allow for a comprehensive machine learning analysis of the dynamics and mechanisms of the SCN (Figure 1A; Table S1).

After multiscale Ca^{2+} signals were preprocessed, we hypothesized that SCN neurons would maintain a stable functional state over short intervals (e.g., 5 min)[10] and focused on neural spatiotemporal states (ST states) as a starting point. To classify ST states by incorporating biological priors, such as a 24-h circadian cycle, spatial similarity of neighboring neurons, and temporal similarity across consecutive time points,[1,2,7,9–11,22–24] we defined a data-adaptive distance metric for *k*-means clustering, which was a combination of three distances over Ca^{2+} signal representations S that were extracted from a spiking autoencoder, circadian phase Φ, and spatial coordinate X (Figure 1B; Table S2; see methods for details). Building on the ST-state clustering results, we further conducted neuron-subtype clustering on the basis of state-switching dynamics (Figure 1B).

Next, we employed time prediction experiments (Figure 1C; see methods for details) using a convolutional neural network (CNN)-based model for ipsilateral and contralateral time predictions, considering the identified subtypes to assess whether these neuron subtypes differ in their time-computation properties.

Finally, after mapping the ST states and neuron subtypes to explicitly defined Ca^{2+} features, we used an ADNN to attribute inter-ST-state and inter-neuron-subtype differences to key signal features and gain biologically meaningful interpretations (Figure 1D; Tables S3 and S4; see methods for details).

Hemispheric asymmetry revealed by ST states and subtypes

Using the newly developed prior-guided clustering method combined with the existing elbow method[25] and the Bayesian information criterion (BIC),[26] we identified four ST states from multiscale Ca^{2+} signals in the SCN (Figures 2A and S1). On average, they accounted for 27.6%, 30.4%, 21.3%, and 20.7% of all Ca^{2+} signals for mice in the 3D-t dataset, with proportions of 28.8%, 28.9%, 20.5%, and 21.8%, respectively, observed in a representative SCN slice (Figure 2B). The four ST states exhibited evident hierarchical differences in both the mean amplitudes and variance of Ca^{2+} signals (Figures 2C and 2D; Table S5). Within an entire circadian period, the dwell times were 6–8 h for states I and II and 8–12 h for states III and IV (Figure 2E). By mapping

Please cite this article in press as: Zhang et al., Interpretable machine learning reveals hemispheric asymmetry of state switching in the suprachiasmatic nucleus, Patterns (2026), https://doi.org/10.1016/j.patter.2026.101617

CellPress
OPEN ACCESS

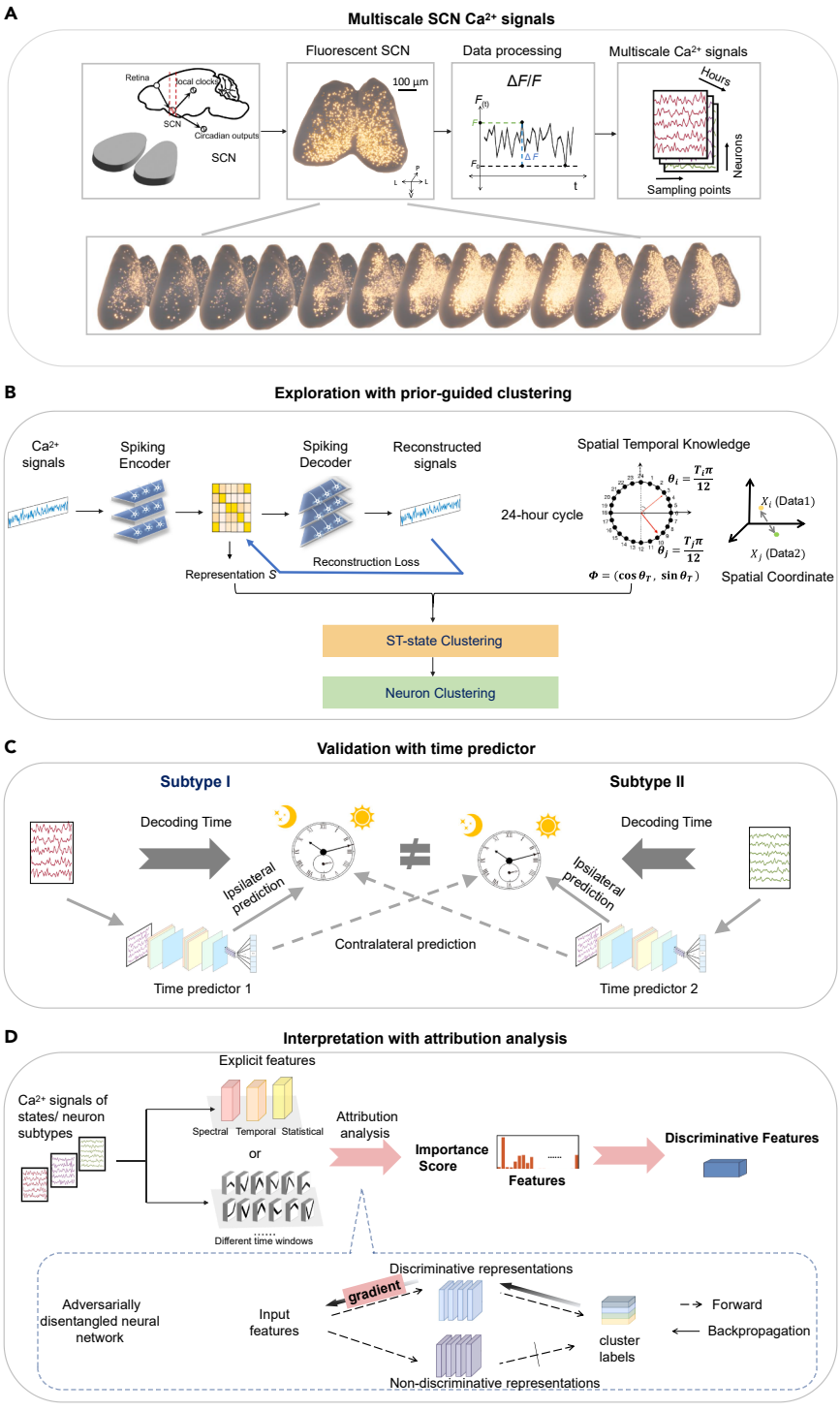

Figure 1. Machine learning-based decoding of SCN spatiotemporal dynamics

(A) Multiscale Ca^{2+} signal processing pipeline. From left to right: cartoon illustration of the acute SCN slice, spatiotemporal Ca^{2+} dynamics (scale bar, 100 μm), Ca^{2+} signal normalization ($\Delta F/F = [F_{(t)} - F_0]/F_0$, F_0: baseline fluorescence), and schematic of multiscale Ca^{2+} signals.

(B) Prior-guided ST-state clustering and neuron clustering. An unsupervised spiking autoencoder extracts low-dimensional embeddings from Ca^{2+} signals. ST-state clustering integrates (1) latent representations, (2) circular sinusoidal embeddings of the circadian phase, and (3) neuronal spatial coordinates.

(C) Subtype-specific time prediction experiments. Subtype-trained CNNs predict circadian time for ipsilateral or contralateral Ca^{2+} signals.

(D) Attribution analysis through ADNN. We calculated the feature importance as the average gradient through discriminative representations in the ADNN and identified key discriminative features and critical time windows associated with the observed patterns.

the ST states to the SCN space, we found that states I and II were ubiquitously distributed across both sides of the bilaterally symmetric nucleus, whereas states III and IV were each unilaterally localized (Figure 2F), indicating the robust hemispheric asymmetry of the SCN.

We next examined the inter-state-switching kinetics. At the population level, all SCN neurons exhibited near-synchronized transitions (hour-scale resolution) between the ST states, with characteristic state splitting occurring mostly during the subjective day (circadian time [CT]1–CT12) (Figure 3A). Apart from temporal variations across slices, all five SCN slices followed a conserved inter-state-switching trajectory. In three out of five slices, the initial phase corresponded to state II and was followed by a synchronized transition to state I at approximately CT20. Subsequent hemispheric asymmetry emerged at CT24–CT26, during which neurons split into states III (51.9% ± 1.4%) and IV (48.1% ± 1.4%) across the two hemispheres (Figure 3B). This pattern persisted for ~12 h before reverting to state II at CT34–CT38. Notably, this near-equilibrium allocation showed a <0.8-h standard deviation (SD) in the timing of state splitting within a representative slice. In the other two slices, this hemispheric asymmetry occurred approximately 3 h later (CT27–CT29), and inter-state switching appeared to be fluttered rather than all synchronized. However, one 3D-t slice exhibited complex ST-state dynamics; although the hemispheric segregation of states III and IV was largely retained (Figure S2), we excluded this slice from further analysis.

Given the ST-state clustering results, we further performed clustering analysis to identify functional neuron subtypes. Specifically, functional neuron subtypes were typically identified using K-modes clustering,[27] in which the 24-h ST states of each neuron were treated as its feature vector. This analysis revealed two distinct functional neuron subtypes, each corresponding to

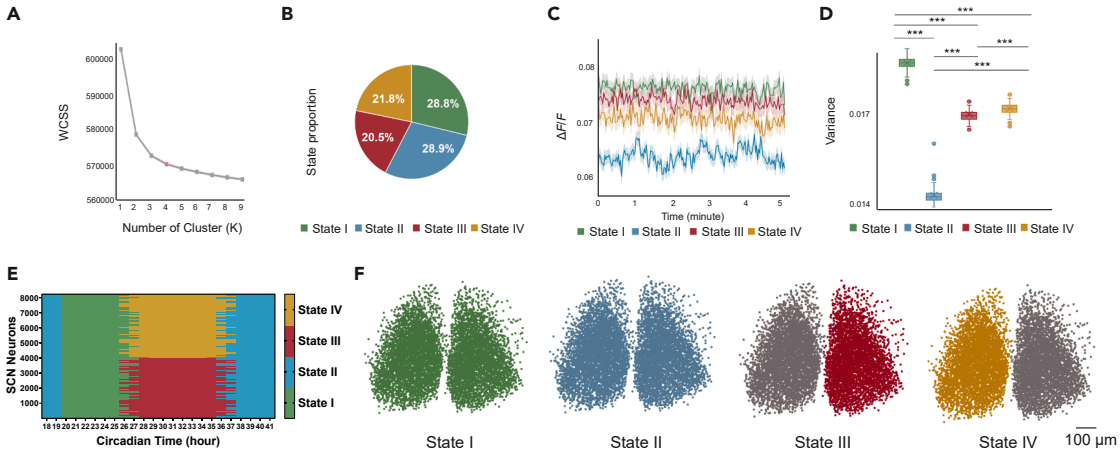

Figure 2. ST-state analysis reveals hemispheric asymmetry in the SCN

ST-state analysis in a representative 3D-t slice.

(A) Cluster number determination via the elbow method. The within-cluster sum of squares (WCSS) plateaus at K = 4, defining four optimal ST states.

(B) Pie chart showing the proportions of the four ST states.

(C and D) Hierarchical differences in mean $\Delta F/F$ with 95% confidence intervals and variance across ST states. The color codes of the ST states are shown at the bottom. $^{*}p < 0.05$, $^{**}p < 0.01$, and $^{***}p < 0.001$ by two-sample *t* test analysis with Bonferroni correction for multiple comparisons.

(E) Raster plot of state switching over 24 hours. The color codes of the ST states are shown on the right.

(F) 3D spatial mapping of the ST states. Scale bar, 100 μm.

a unique state-switching trajectory (Figure 3A). Spatial mapping of these neuron subtypes revealed a structured architecture along the left-right axis, further supporting the presence of hemispheric asymmetry in the SCN (Figure 3C).

Since the ST-state analysis and the subsequent neuron subtype classification integrated Ca^{2+} signal features with spatiotemporal priors, we performed ablation experiments to evaluate the contributions of the three components—namely, Ca^{2+} signal representations (S), temporal priors (Φ), and spatial priors (X)—to the clustering outcomes and, in particular, to hemispheric asymmetry. Clustering based solely on Ca^{2+} signal representations revealed some asymmetrically distributed spatial clusters (Figure S3A), whereas clustering based only on spatiotemporal priors produced a predominantly circadian phase-driven pattern, with neurons switching near synchronously between discrete states lasting ~5–7 h each (Figure S3B). The incorporation of Ca^{2+} signal representations with the temporal prior yielded a similar pattern, with neurons synchronously switching between discrete states, each lasting for 6 h (Figure S3C). In contrast, incorporating Ca^{2+} signal representations with the spatial prior resulted in four neuron classes that remained in stable states throughout the circadian cycle, and their spatial map exhibited both left-right and dorsal-ventral asymmetry (Figure S3D). After all the components were integrated, left-right hemispheric asymmetry emerged as a prominent feature of the SCN (Figure 3). Given that the temporal prior weights each circadian hour equally, the emergence of asymmetric states specifically during the subjective day is unlikely to be driven by spatiotemporal priors alone. Instead, this pattern emerged after integrating Ca^{2+} signal representations with spatial and temporal priors, suggesting that Ca^{2+} activity contributes to stronger hemispheric asymmetry during the subjective day.

We further performed a permutation-based feature importance assessment to demonstrate the influence of each component on the clustering results. Shuffling any individual component generally resulted in clustering outcomes that were less similar to our original clustering result and exhibited poorer clustering quality metrics (see methods and Table S6 for details). These results suggested that each component contributed to the clustering result and that our raw clustering result was reasonable.

For all five slices examined, hemispheric asymmetry occurred during the subjective daytime. To validate the robustness of our findings at finer scales, we analyzed three additional 2D-t SCN datasets, featuring noninterruptive, higher-frequency sampling over time windows of several hours during the day (CT7–CT11, CT10–CT12, and CT9–CT13, respectively; Table S1), when states III and IV coexisted (Figure 3A). Leveraging the above prior-guided clustering approach, we segmented the Ca^{2+} signals into contiguous 5-min intervals, performed clustering for two ST states corresponding to the states at the same time in the 3D-t data, and then extracted state distributions and neuron subtypes on the basis of state-switching patterns. Our results revealed that, in this high-temporal-resolution dataset, the two ST states or neuron subtypes corresponded to either side of the SCN (Figure 4), and there was no state switching in individual neurons during the observation period. These results reinforced the robustness and stability of the hemispheric asymmetry of the SCN during the subjective day.

Side-specific timekeeping properties

Previous studies have demonstrated that in constant light (LL)-induced rhythm splitting, the left and right SCNs of hamsters exhibited antiphase oscillations in clock gene expressions,[28–30] whereas mice under LL conditions exhibited coherent *Per1* gene expressions within individual SCN nuclei but 12-h antiphase oscillations between hemispheres.[31] These phenomena were modeled into coupled evening (E) and morning (M) oscillators, indicating that each SCN hemisphere independently drives

Please cite this article in press as: Zhang et al., Interpretable machine learning reveals hemispheric asymmetry of state switching in the suprachiasmatic nucleus, Patterns (2026), https://doi.org/10.1016/j.patter.2026.101617

CellPress
OPEN ACCESS

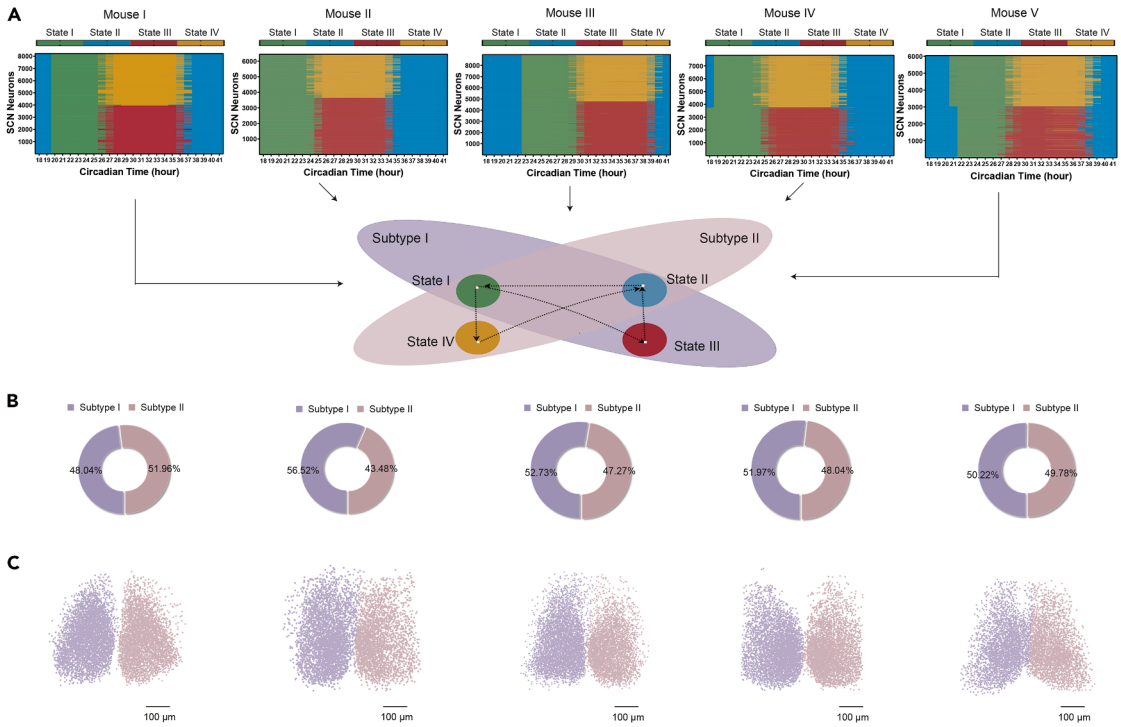

Figure 3. Functional neuron subtypes revealed by ST-state switching

(A) State switching over 24 h of all five 3D-t SCN slices. The images at the top are the raster plots, and the ST state color codes are shown above. The image on the bottom is the trajectory of inter-ST-state switching. Subtype I: state II → state I → state III → state II; subtype II: state II → state I → state IV → state II.

(B) Proportions of the two identified SCN neuron subtypes.

(C) 3D spatial mapping of functional neuron subtypes in the SCN space. The same-type neurons were predominantly located on either the left or the right side of the SCN. Scale bar, 100 μm.

behavioral outputs.[28,32,33] Moreover, rats exposed to an artificially short 22-h LD cycle displayed antiphase neural activities between the ventral and dorsal SCN regions.[34] Our findings extend these insights by leveraging multiscale neuronal activity data to elucidate the hemispheric asymmetry in mouse SCN slices under free-running conditions, suggesting that hemispheric asymmetry is a fundamental property that is intrinsic to the circadian clock.

We have recently shown that a properly trained CNN can faithfully predict circadian time with hourly precision by polling just a few hundred randomly selected SCN neurons.[10] To explore how asymmetry affects time computation and representation in the SCN, we generated subtype/side-specific time predictors by training models exclusively on Ca^{2+} signals from one subtype (Figures 5A and 5B). These time predictors were then applied to both subtypes to test and compare their performance with that of either subtype. Given the spatial asymmetry of subtypes, this is equivalent to testing the performance of ipsilateral and contralateral time prediction. That is, we leveraged the time predictor as an investigative tool to reveal potential side-specific differences in timekeeping.

The results revealed that ipsilateral time prediction achieved an accuracy greater than 99% when a random cohort of 900 neurons was polled (Figures 5C and 5D), indicating that each functional neuron subtype encodes a complete time feature representation. In contrast, the average accuracy of the contralateral time predictions was markedly lower (44.9% ± 5.6%; mean ± SEM, n = 10). The difference between the ipsilateral and contralateral testing accuracy suggested distinctive side-specific time representations (Figures 5C, 5D, S4A, and S4B). At the hour level, contralateral time prediction revealed pronounced oscillatory behavior, with the accuracy alternating between peaks (>99%) and troughs (<10%) (Figures 5E and S4C). Despite their relative independence, both hemispheres exhibited closely aligned in-phase oscillatory fluctuations in contralateral time predictability (average cosine similarity = 0.85; n = 5 mice). Intriguingly, the peaks in the contralateral time-prediction accuracy were temporally aligned with vertical bands in Ca^{2+}-signal-representation-only raster plots (Figures 5E and S4D). These vertical bands indicate time windows in which more neurons were assigned to similar states, suggesting increased cross-hemispheric similarity that facilitates contralateral prediction. Together, these results suggest that high ipsilateral predictability reflects the coupled dynamics within each SCN hemisphere, whereas interhemispheric coupling may serve to align the circadian phase and maintain coherent timekeeping.

Ca^{2+} features underlying hemispheric asymmetry

Hemispheric asymmetry was identified from the integrated clustering results of the neuron subtypes and ST states. To further explore which features of Ca^{2+} signals were associated with this asymmetry, we performed attribution analysis for a

Please cite this article in press as: Zhang et al., Interpretable machine learning reveals hemispheric asymmetry of state switching in the suprachiasmatic nucleus, Patterns (2026), https://doi.org/10.1016/j.patter.2026.101617

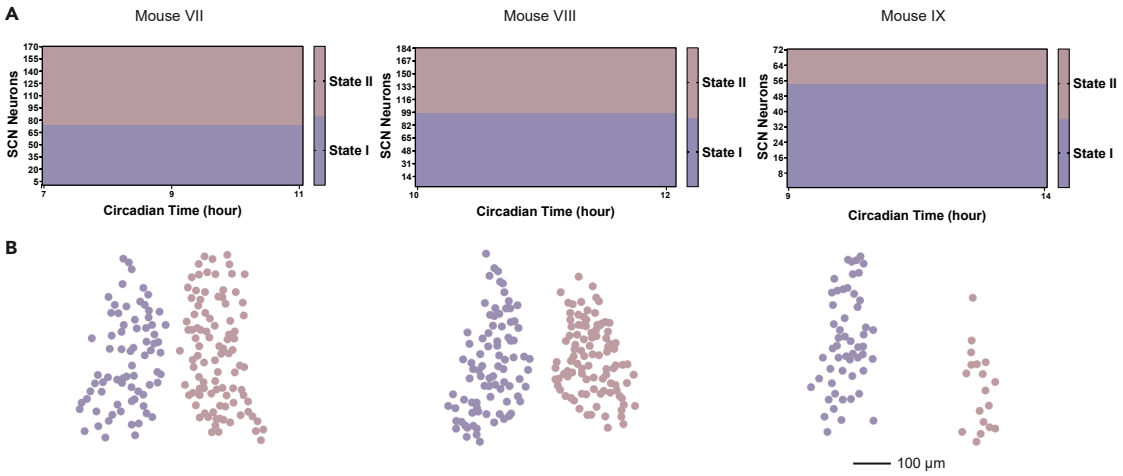

Figure 4. Analysis of high-temporal-resolution 2D-t data validated hemispheric asymmetry in the SCN

(A) Raster plots of ST-state switching.

(B) Spatial mapping of the neuron subtypes in the SCN space. Scale bar, 100 μm.

representative sample with an ADNN in which the contribution coefficients of Ca^{2+} features to the clustering results were calculated and key Ca^{2+} features were identified (Figure 6A; see methods for details). We found that spectral features emerged as major discriminative elements associated with hemispheric asymmetry, alongside contributions from temporal and statistical features. Specifically, the top 20 features that are critical for inter-subtype differentiation included the fast Fourier transform (FFT) mean, especially during the subjective day, kurtosis, etc. (Figure 6B). The FFT frequencies that contribute to hemispheric asymmetry range from 0 to 0.33 Hz (Figure 6C), falling within the range of Ca^{2+} oscillations previously reported in SCN neurons and astrocytes.[10,35–37] These include Ca^{2+} transients with periods of approximately 10–100 s (0.01–0.1 Hz) in neurons and 7–70 s (0.014–0.14 Hz) in astrocytes.[36] This frequency band also corresponds to the irregular firing of spontaneous action potentials in SCN neurons, which occurs at 0–3.5 Hz.[38,39] Additionally, the amplitude differences observed between subtypes I and II (Figures 6B and 6D) were primarily attributed to kurtosis, a statistical feature indicative of nested oscillatory structures,[40] with elevated kurtosis reflecting a higher intensity of Ca^{2+} bursts during slow oscillatory cycles.

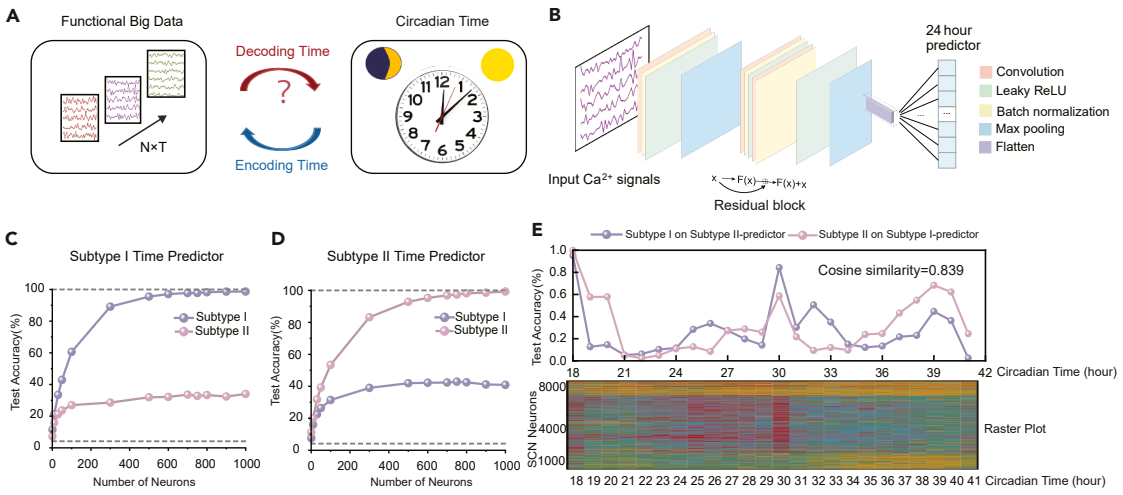

Figure 5. Subtype-specific time prediction experiments revealed the time encoding properties of the SCN hemispheres

(A) Decoding time from circadian Ca^{2+} dynamics across neuronal populations. By testing the time decoding performance with time predictors trained with different subsets of data, we aimed to infer side-specific differences in the time-encoding mechanism.

(B) The residual CNN[10] trained for time prediction to validate hemispheric asymmetry in the SCN.

(C and D) Ipsilateral time predictability from CNNs trained with Ca^{2+} signals from one side (C) or the contralateral side (D). The bottom dashed line represents the chance level.

(E) Hour-level contralateral time predictability and corresponding Ca^{2+}-signal-representation-only state-switching raster plot. Top: hour-level contralateral time predictability exhibiting in-phase oscillatory behavior (n = 100 neurons). Bottom: Ca^{2+}-signal-representation-only raster plot showing state-switching patterns over circadian time.

Please cite this article in press as: Zhang et al., Interpretable machine learning reveals hemispheric asymmetry of state switching in the suprachiasmatic nucleus, Patterns (2026), https://doi.org/10.1016/j.patter.2026.101617

CellPress
OPEN ACCESS

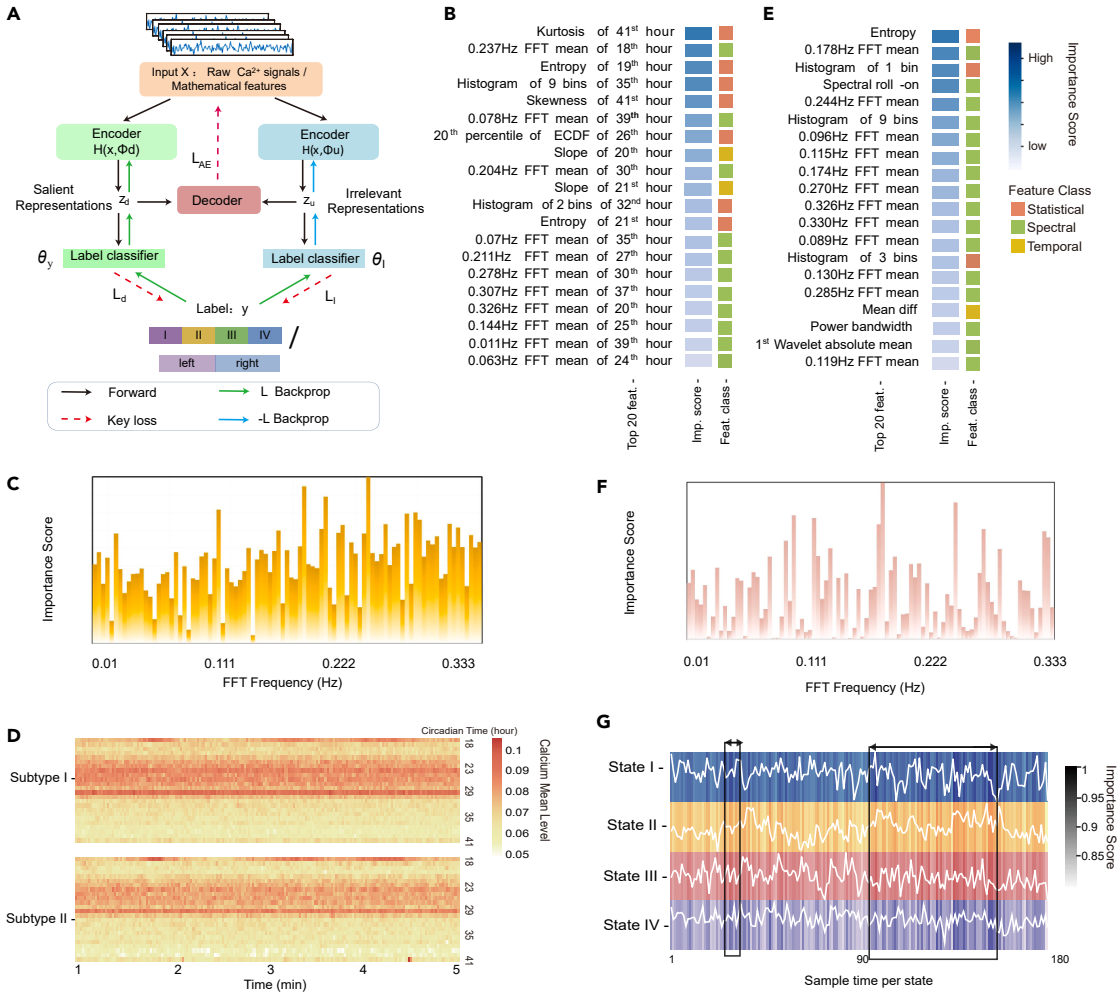

Figure 6. Attribution analysis revealed deterministic features associated with hemispheric asymmetry in the SCN

Similar results are obtained across all the samples.

(A) Schematic of the ADNN for attribution analysis.

(B–D) Attribution analysis for the neuron subtypes.

(B) Feature importance score and the top 20 features for distinguishing different neuron subtypes.

(C) Importance scores of the FFT mean features with different frequencies.

(D) The mean Ca^{2+} signal amplitude of each neuron subtype.

(E and F) Attribution analysis for the ST states.

(E) Feature importance score and the top 20 features for distinguishing different ST states.

(F) Importance score of the FFT mean features with different frequencies.

(G) Attribution analysis for the most important time windows.

Similar patterns were observed in the attribution analyses of the ST states, supporting the association between the spectral components and the identified asymmetry. Specifically, the top 20 features included the FFT mean features, entropy, etc. (Figure 6E). We demonstrated that spectral features accounted for the greatest proportion of the top 20 contributors across all five mice. The visualization of the importance score for the FFT mean features with different frequencies is shown in Figure 6F, and the interpretation was similar to and consistent with that of the above inter-subtype attribution analysis. Entropy, previously used to quantify the irregularity or complexity of neuronal activity in the SCN,[41] emerged as a key feature distinguishing inter-ST-state differences in our analysis (Figure 6E). We also identified key time windows in the Ca^{2+} time series that were critical for clustering ST states. Attribution analysis of the raw Ca^{2+} time series revealed that the curve trends varied between ST states in several important time windows, which are marked in the boxes (Figure 6G). Similar results were obtained across all five slices analyzed (Figure S5).

DISCUSSION

Although tens of thousands of heterogeneous SCN neurons act as an integrated unit to compute and represent physical time, a comprehensive, system-level understanding of how this neuron ensemble functions remains elusive. Progress in this direction

Please cite this article in press as: Zhang et al., Interpretable machine learning reveals hemispheric asymmetry of state switching in the suprachiasmatic nucleus, Patterns (2026), https://doi.org/10.1016/j.patter.2026.101617

has been hindered by three major challenges: the scarcity of neuron-resolved, circadian-scale datasets; the lack of mathematical tools capable of extracting the full informational richness of such datasets; and, to a lesser extent, the computational power that is required to support large-scale, data-driven analyses. To address these gaps, we developed an interpretable machine learning framework to decode neuronal Ca^{2+} signals by integrating spatial and temporal considerations. This framework combines prior-guided ST-state and subtype clustering for pattern identification, CNN-based time prediction for validation, and ADNN-based attribution for mechanistic interpretation. While not establishing strict causality, this framework offers a comprehensive analytical strategy for understanding SCN dynamics and lays the groundwork for further exploration of the functional organization of the mammalian circadian clock.

The application of this framework to large-scale SCN Ca^{2+} datasets extended single-cell observations into long-term, neuron-resolved population analyses, enabling the detection of network-level transitions and revealing large-scale organizational patterns. Hemispheric asymmetry was revealed as an intrinsic feature of the SCN architecture, manifested by two neuron subtypes with unidirectional state-switching patterns and by two of the four ST states exhibiting mutually exclusive hemispheric segregation during the subjective day in 8 out of 9 slices. Notably, the timing of hemispheric lateralization is roughly aligned with the phase wave of hyperactivity (PWHA) reported previously.[10] These ST states, derived from multiscale Ca^{2+} dynamics and constrained by circadian and spatial priors, are conceptually distinct from the classical membrane-potential states characterized electrophysiologically[42–46]; however, both types of analyses emphasize that SCN neurons switch between discrete states across the circadian timescale. The timekeeping properties of this asymmetry were further confirmed using CNN-based time predictors: models trained on hemispheric Ca^{2+} signals accurately predicted ipsilateral time but performed poorly in contralateral prediction. Notably, the contralateral time prediction accuracy exhibited large oscillations between near-perfect and near-zero on a timescale of several hours, showing that each hemisphere computes time but still couples in concert with its counterpart. Finally, attribution analysis demonstrated that the spectral, temporal, and statistical features of Ca^{2+} signals are major discriminative elements associated with distinguishing both inter-ST-states and inter-neuron subtypes, with spectral features playing the dominant role. These findings support a model in which SCN hemispheres act as independent but coupled oscillators—an asymmetrically organized architecture that bolsters the precision and flexibility of circadian timekeeping.

Lateralization of brain function is widely observed across multiple brain regions, including the amygdala,[47] hippocampus,[48] and whole-brain networks.[49] In the SCN, earlier studies reported antiphase clock gene rhythms between the left and right nuclei in behaviorally splitting animals under LL conditions, a phenomenon conserved across rodent species.[31,34] Although early evidence suggested that one SCN hemisphere is sufficient to sustain daily rhythms in rodent behavior,[50] more recent studies have shown that unilateral SCN lesions can alter reproductive indices,[51] as well as the subregion "splitting" within the unilateral SCN, where ventrolateral and dorsomedial subregions oscillate in antiphase with an ~12-h phase difference.[52–55] Moreover, we and others have reported that PWHA traverses the entire SCN on a circadian timescale and that the wavefront generally propagates symmetrically with subtle hemispheric differences.[10,56] In contrast, our machine learning-based analysis of Ca^{2+} dynamics revealed, for the first time, hemispheric asymmetry in free-running SCN slices. We speculate that these hemispheric differences may reflect the intrinsic physiology of the SCN hemispheres, whereas coordinated interactions may support coherent circadian regulation of the whole organism. In intact animals, particularly under specific conditions (e.g., LL), such asymmetry may be enhanced by inherently lateralized inputs from the retina[57,58] and raphe,[59] which generate lateralized photic and neuromodulatory signaling, resulting in regional splitting and even hemispheric uncoupling.

Intriguingly, the phase of the hemispheric asymmetry coincides with the dead zone of the phase response curve, during which no phase shifts are induced by light.[60,61] This observation suggests that the dead zone may represent a paradoxical condition in which cellular phase stability coexists with partially independent hemispheric coupling, allowing the SCN to be transiently isolated from environmental perturbations. The few-hour alternation between SCN synchrony and lateralization likely reflects the dynamic modulation of interhemispheric coupling strength, enabling flexible adaptation to photic inputs and providing an efficient strategy to regulate network dynamics. Moreover, the efficacy of clock-modulating drugs depends on dosing timing, environmental cues, and molecular factors.[62,63] In this context, the network state is also likely a modulator of drug outcomes. Together, these observations suggest that photic input acts as a key factor underlying SCN hemispheric asymmetry. If prolonged light exposure amplifies this asymmetry, the present results may provide a physiological basis for previously reported circadian rhythm splitting under LL.

In summary, this study reveals hemispheric asymmetric timekeeping features of the master circadian clock in mice using interpretable machine learning. This hemispheric asymmetry appears to be a dynamic process, waxing and waning on several-hour scales, suggesting dynamic coordination between the SCN hemispheres. This aligns with broader principles observed in other brain regions, such as the cortex, where functional lateralization arises from asymmetric cross-hemispheric communication and supports specialized processing and cognitive flexibility.[64] Further studies are warranted to elucidate the underlying mechanism and biological role of hemispheric asymmetry in circadian timekeeping.

METHODS

Experimental model and study subject details

All animal experiments were conducted in accordance with the guidelines of the Animal Care and Use Committee of Peking University, accredited by AAALAC International, and the procedures were approved by the Animal Care Committee of the PKU-Nanjing Institute of Translational Medicine (approval ID: IACUC-2021-023). All mice were housed at 20°C–22°C under a 12-h LD cycle, with *ad libitum* access to water and food. *Viaat-Cre::GCaMP6s* mice or *Viaat-Cre::GCaMP6f* mice were generated by crossing *Viaat-Cre* mice (JAX #017535)[65] with *Rosa26-LSL-GCaMP6s*

mice[66] or *Rosa26-LSL-GCaMP6f* mice (JAX #024105)[67] for at least two generations.

The preparation and Ca^{2+} imaging of SCN slices were performed as previously described.[10] Briefly, 8-week-old male mice exhibiting robust rhythmic activity were sacrificed at zeitgeber time 11 for slice preparation. Volumetric Ca^{2+} imaging of entire 300-μm SCN slices was then conducted using a dual-objective two-photon microscope[68] at a rate of ∼0.67 volumes/s for 5 min, with a total imaging duration of 30 h from CT12 to CT41. Continuous single-plane Ca^{2+} imaging of SCN slices was conducted using the same microscope at a rate of 2.7 Hz for several hours. See Table S1 for details of the dataset.

The structure of the prior-guided clustering model

The prior-guided clustering model designed a data-adaptive distance metric to integrate Ca^{2+} signal representations, temporal priors, and spatial priors for ST-state analysis, with Ca^{2+} signal representations extracted using a spiking autoencoder and the priors biologically informed. Below, we explain these steps in more detail.

Spiking autoencoder to extract the representations of Ca^{2+} signals

Our spiking autoencoder consisted of a spiking encoder and a spiking decoder. The spiking encoder converted the Ca^{2+} signal into latent representations and minimized the noise in the raw Ca^{2+} signals, whereas the spiking decoder reconstructed the Ca^{2+} signal from the latent representations. Compared with traditional neural networks, spiking autoencoders can process brain signals more efficiently and with potentially reduced energy consumption.[69–71]

Our spiking autoencoder was composed of leaky integrate-and-fire (LIF) spiking neurons,[72] which were modeled as follows:

$$\tau_m \frac{du(t)}{dt} = -(u(t) - u_{rest}) + RI(t), u(t) < V_{th}, \quad \text{(Equation 1)}$$

where $u(t)$ represents the membrane potential of each neuron of the spiking autoencoder, $I(t)$ represents the input of each neuron of the spiking autoencoder, V_{th} represents the firing threshold of our spiking autoencoder, and R and τ_m represent the resistance and leakage terms, respectively. When $u(t)$ reaches V_{th} at time t_f, the neuron of the spiking autoencoder emits a spike and resets the membrane potential $u(t)$ to u_{rest}, which is set to 0. The output spike train of a neuron is represented by $s(t) = \sum_{t_f} \delta(t - t_f)$, where δ is the Dirac function. For the network model, the neurons are connected by weights w, and we considered the simple current model $I_j[t] = \sum_i w_{ij} s_i[t] + b_j$. The discrete computational form of the network is as follows:

$$\begin{cases} u_j[t+0.5] = \lambda u_j[t] + \sum_i w_{ij} s_i[t] + b_j \\ s_j[t+1] = H(u_j[t+0.5] - V_{th}) \\ u_j[t+1] = u_j[t+0.5] - V_{th} s_j[t+1], \end{cases} \quad \text{(Equation 2)}$$

where $H(x)$ denotes the Heaviside step function, $s_i[t]$ is the binary spike train of neuron i, λ is a leaky term related to the constant τ_m and the discretization time interval for the LIF model, and we use subtraction as the soft reset.

The specific spiking autoencoder structure is shown in Table S2, and it was trained to learn the model parameter w using backpropagation through time (BPTT) and a surrogate gradient[73] to minimize the mean squared error (MSE) loss using the Adam optimizer[74] for 5 epochs. The learning rate was set to 0.005. The spiking autoencoder was developed using the SpikeJelly framework.[72]

Prior-guided clustering

Considering both temporal and spatial interactions in the dynamics of the SCN nucleus, we developed a clustering approach using spatiotemporal information for Ca^{2+} signal analyses. We considered three components in the clustering: (1) 150D latent Ca^{2+} signal representations S extracted from a spiking autoencoder, (2) 3D spatial coordinates X, and (3) 2D circadian temporal information Φ. The 2D circadian temporal information of states within the i^{th} hour was represented by $\Phi_i = \left(\sin\left(\frac{i\pi}{12}\right), \cos\left(\frac{i\pi}{12}\right)\right)$, mapping time onto a circular space. This new temporal representation solved boundary discontinuities inherent to linear hour indices (e.g., the separation of hours 24 and 1 under linear hour indices) by enforcing cyclic continuity.

The analysis was performed using a 24-h cycle prior and spatiotemporal priors, which are based on the assumption that neighboring neurons and consecutive time points exhibit consistent state distributions. This assumption served as a mathematical simplification, where the same subtypes aggregate spatially as functional and structural modules within the SCN,[10,11] and temporally, it corresponds to the sequential activation of neuronal assemblies in the SCN.[1,2,7,9,22–24]

To incorporate the above priors into the clustering method, we propose a new distance metric for the k-means clustering algorithm. As shown in Equation 3, the distance metric considered different distance components of three kinds of features: 150D Ca^{2+} signal representations S, 2D circadian phase vectors Φ, and 3D Euclidean spatial coordinate vectors X.

$$d(i,j) = \lambda_S \|S_i - S_j\|_2 + \lambda_\Phi \|\Phi_i - \Phi_j\|_2 + \lambda_X \|X_i - X_j\|_2. \quad \text{(Equation 3)}$$

Our distance metric adaptively balanced the three terms, which set the balance parameters of the three terms as $\lambda_S = \frac{a}{M_S}$, $\lambda_\Phi = \frac{a}{M_\Phi}$, and $\lambda_X = \frac{a}{M_X}$, where M_S, M_Φ, and M_X were the SDs of the Ca^{2+} signal representations, circadian temporal vectors, and spatial vectors, respectively, as shown in Equation 4. a can be chosen as any positive constant, and we choose $a = M_\Phi$, i.e., $\lambda_\Phi = 1$, so that we can compare the parameters of different mice.

$$M_S = \sqrt{E\|S_i - S_j\|_2^2} = \sqrt{2}\sqrt{E\|S - \mathrm{E}[S]\|_2^2} = \sqrt{2}SD(S),$$
$$M_\Phi = \sqrt{E\|\Phi_i - \Phi_j\|_2^2} = \sqrt{2}\sqrt{E\|\Phi - \mathrm{E}[\Phi]\|_2^2} = \sqrt{2}SD(\Phi), \text{and}$$
$$M_X = \sqrt{E\|X_i - X_j\|_2^2} = \sqrt{2}\sqrt{E\|X - \mathrm{E}[X]\|_2^2} = \sqrt{2}SD(X). \quad \text{(Equation 4)}$$

Therefore, the distance metric can be represented as $d(i,j) = a\left(\frac{\|S_i - S_j\|_2}{M_S} + \frac{\|\Phi_i - \Phi_j\|_2}{M_\Phi} + \frac{\|X_i - X_j\|_2}{M_X}\right)$. This distance with a data-adaptive parameter ensures that all the terms have the

same scale and contribute equally to the clustering, with no one term dominating. This method also eliminates the need for hyperparameter tuning.

After ST-state clustering, we performed neuron clustering on the basis of the state-switching results. The feature vector of each neuron was composed of the neuron's 24-h ST-state sequence. We chose the Hamming distance as the distance metric because the feature vector component was categorical. We subsequently performed K-modes clustering[27] through the neuronal dimension to obtain the neuron subtypes. The entire clustering method was data adaptive and automatic. To better capture the state-switching property when there was noise in the switching times, we also used the switching sequence, which was calculated by compressing the state sequence. We subsequently applied k-medoids clustering to the state-switching sequences using the Levenshtein distance. This method was more robust when there was noise in the switching times and produced results consistent with our results in the manuscript.

To verify the hemispheric asymmetry, we also analyzed the 2D-t dataset, which reflected continuous records of several hours during the subjective day (Table S1). Using the prior case in which two states coexisted during the subjective day (Figure 3A), we set the number of *k*-means clusters to 2. We divided the Ca^{2+} signals into contiguous 5-min segments and set $\Phi_i = \left(sin\left(\frac{(T+i/12)\pi}{12}\right), cos\left(\frac{(T+i/12)\pi}{12}\right)\right)$, where T was the start hour of the recording. We used our method for this new dataset and calculated the SDs of all Ca^{2+} signal representations, 24-h circadian temporal vectors, and all spatial vectors as M_S, M_Φ, and M_X, respectively. We then applied the K-modes algorithm to the state clustering results in the spatial dimension, and the SCN clustering results are shown in Figure 4. The state and neuron subtype patterns of all three mice were consistent with the 3D-t data.

Calculation of Cohen's d effect size

We calculated the effect size measurement, Cohen's d, together with confidence intervals for the variance of the Ca^{2+} signal using the R package effsize.[75] An absolute value of Cohen's d greater than 0.8 is considered a large effect size.[76,77]

Attribution analysis with ADNN

We aimed to identify the key "biomarkers" of different ST states or neuron subtypes. Therefore, we first used the tsfel[78] package to extract meaningful features of each state, which includes more than 200 different features in the statistical, temporal, and spectral domains, such as the median, autocorrelation, mean, variance, kurtosis, and FFT mean coefficient. We also used the tsfel package to extract the features of each neuron subtype, which includes more than 5000 different features in the statistical, temporal, and spectral domains, such as the maximum Ca^{2+} signals in the 21st hour and the skewness of the 32nd hour. These features differ from the raw Ca^{2+} signals or representations and can provide more explanations.

To extract the contribution coefficient of each feature and explore the key discriminative features of the four ST states or two SCN subtypes, we built a gradient-based attribution analysis method while further designing the ADNN for better identification. The attribution analysis first trains a neural network model for classification and then calculates the gradients of inputs to identify the contributions of each component. Unlike the vanilla method, our algorithm comprehensively decoupled the representations of the neural network model into discriminative representations and non-discriminative representations for more reliable attribution. We split the representations into two parts, where the discriminative component was encouraged to accurately predict the Ca^{2+} categories (ST state or neuron subtype), while the other component was forced to fail for predictions through adversarial optimization. The ADNN was implemented utilizing two encoders that transferred raw data to the low-dimensional latent space and a decoder that reconstructed raw data from latent representations. The two encoders learned discriminative representations and non-discriminative representations through the downstream classification task and adversarial optimization, respectively. The discriminative representations and non-discriminative representations were merged and input into a common decoder for the reconstruction of raw data. The loss of an ADNN was composed of reconstruction loss, classification loss, and adversarial loss. The network structure can be found in Table S3, and the specific training algorithm can be found in Box 1. We trained the ADNN to solve the key min-max optimization problem, $\max_{\Phi_u} \min_{\theta_l} L_l$, where L_l is the cross-entropy loss of the non-discriminative branch, and the other parameters are defined in Box 1.

To assess the extent to which the Ca^{2+} features reflected general lateralization properties, we trained an ADNN to classify different neuron subtypes. Our method achieved a test accuracy of 71% on a held-out test set. This is substantially higher than chance (a baseline accuracy of 50%) and supports the idea that hemispheric asymmetry was reflected in the Ca^{2+} signal features. The test accuracy is also better than that of a standalone classifier (66%), which is a linear classifier trained on the same features. The superior performance of our approach demonstrates enhanced feature generalizability and suggests more plausible attribution mechanisms.

We also calculated the classification accuracy and Cohen's kappa for the ST states. The classification accuracy is 35.42%, which is greater than chance (a baseline accuracy of 25%). The Cohen's kappa between our methods and ground truth is 0.14, indicating some level of agreement that exceeds random guessing.[79]

To determine which mathematical features/which parts of Ca^{2+} signals are most relevant to the essence of different states/different SCN subtypes, we used gradient-based attribution for the classification loss of the ADNN. We used a gradient measure r_i that averages the gradient of the loss L with respect to a given input characteristic x_i through the discriminative features C over all of the examples x in a dataset X, where x_i is the i^{th} element of x:

$$r_i = \frac{1}{|X|}\sum_{x\in X}\left|\frac{\partial L}{\partial C}\cdot\frac{\partial C}{\partial x_i}\right|. \quad \text{(Equation 5)}$$

Time predictor based on Ca^{2+} signals

Each dataset, i.e., the entire SCN or single-sided subtype-specific Ca^{2+} signals, was divided into training, validation, and testing datasets at a ratio of 6:1:3. The time predictor was

Box 1. Pseudocode of the training algorithm of ADNN

Input: input signal or characteristics x, clustering label y, and convergence iteration number K; ADNN parameters include discriminative encoder ϕ_d and non-discriminative encoder parameter ϕ_u. The classifier g_y with parameter θ_y is in the discriminative branch, and the classifier g_l with parameter θ_l is in the non-discriminative branch. Cross-entropy loss is L_y, reconstruction loss is L_{AE}, and the loss hyperparameters are λ_1 and λ_2.

for iteration k from 0 to K do

Stage 1. min $L_l(\theta_l)$

Forwards through non-discriminative branch

$\widehat{y} = g_l(H_u(x, \phi_u))$.

$L_l = L_y(y, \widehat{y})$

Update non-discriminative feature classifier params

$\theta_l \leftarrow \theta_l - \eta \frac{\partial L_l}{\partial \theta_l}$.

Stage 2. min $\left(L_{AE} + \lambda_1 L_d(\theta_y) - \lambda_2 L_u(\phi_u)\right)$

Forwards through two branches

$z_d = H_d(x, \phi_d), z_u = H_u(x, \phi_u)$.

$\widehat{y}_d = g_y(H_d(x, \phi_d), \widehat{y}_u = g_l(H_u(x, \phi_u)$.

$L_{AE} = \|Decoder(z_d, z_u) - x\|, L_d = L_y(y, \widehat{y}_d), L_u = L_y(y, \widehat{y}_u)$

Update feature extractor and classifier

$$\phi_u \leftarrow \phi_u - \eta\left(\frac{\partial L_{AE}}{\partial \phi_u} - \lambda_2 \frac{\partial L_u}{\partial \phi_u}\right).$$

$$\phi_d \leftarrow \phi_d - \eta\left(\frac{\partial L_{AE}}{\partial \phi_d} + \lambda_1 \frac{\partial L_d}{\partial \phi_d}\right).$$

$$\theta_y \leftarrow \theta_y - \eta\left(\frac{\partial L_{AE}}{\partial \theta_y} + \lambda_1 \frac{\partial L_d}{\partial \theta_y}\right).$$

$$\theta_{Decoder} \leftarrow \theta_{Decoder} - \eta \frac{\partial L_{AE}}{\partial \theta_{Decoder}}.$$

end for

constructed with a CNN.[80] During the time prediction tests, we employed a random selection of neuron cohorts, with each data point averaged across 500 random trials. This setting was consistent with our previous work, and the training and testing details can be found in this paper.[10]

Statistical analysis

Statistical analyses were conducted using Microsoft Excel (Office 2021, Microsoft Corp.) and GraphPad Prism (v.8.3.0, GraphPad Software). The number of independent experiments (n) and the relevant statistical parameters for each experiment, such as the means ± standard errors of the means (SEMs), are described in the manuscript. Between-group comparisons were performed using two-sample t tests in Excel. The normality of the data used in these t tests was validated with the Kolmogorov-Smirnov test. Investigators were not blinded to allocation during the experiments or outcome assessment.

RESOURCE AVAILABILITY

Lead contact

Further information and requests for resources and reagents should be directed to and will be fulfilled by the lead contact, Xiao-Hua Zhou (azhou@math.pku.edu.cn).

Materials availability

The current study has not generated any new material.

Data and code availability

All data used in this study are publicly available as detailed in the methods section. Briefly, 2D-t data are available through Zenodo: https://doi.org/10.5281/zenodo.15817326.[81] 3D-t data[10] and codes used for the analyses are available through Zenodo: https://doi.org/10.5281/zenodo.20637473.[82]

ACKNOWLEDGMENTS

We thank Jinzhuo Wang (Peking University), Jie He (Peking University), Wei Hu (Peking University), Yumou Qiu (Peking University), Cen Yang (Peking University), Haoxiang Wang (Peking University), and Yu Zhu (Institute of Automation, Chinese Academy of Sciences) for critical reading and helpful discussion of the manuscript. We also thank the Biomedical Computing Platform of National Biomedical Imaging Center at Peking University for computational resources. The work is supported by the National Key R&D Program of China (2021YFF0901400), the National Natural Science Foundation of China (62276004, 32293210, and 32327802), the National Science and Technology Innovation 2030 Major Program (2021ZD0202205 and 2022ZD0211903), the CAMS Innovation Fund for Medical Sciences (2019-I2M-5-054), and the Beijing Municipal Science and Technology Commission (Z251100000725008). This research was partially funded by Novo Nordisk A/S.

AUTHOR CONTRIBUTIONS

Conceptualization, H.C. and X.-H.Z.; supervision, H.C. and X.-H.Z.; resources, H.C. and X.-H.Z.; writing – original draft, Zongpeng Zhang and Z.W.; writing – review & editing, H.C., X.-H.Z., Zongpeng Zhang, Z.W., J.Y., M.X., H.L., Zongkun Zhang, X.F., Y.X., L.M., and Z.L.; project administration, H.C. and X.-H.Z.; pipeline design, Zongpeng Zhang, Z.W., and M.X.; methodology and software, Zongpeng Zhang (clustering and attribution), Z.W. (time prediction), M.X., H.L., and Z.L.; investigation, Zongpeng Zhang, J.Y., Y.X., and L.M.; visualization, Zongpeng Zhang and Z.W.; communication and coordination among team members, Z.W.; design and conduct of all animal experiments, J.Y. (design and conduct) and X.F. (conduct); validation, Zongkun Zhang; and valuable suggestions on various aspects of the project, Y.X., L.M., and Z.L.

DECLARATION OF INTERESTS

The authors declare that they have no competing interests.

DECLARATION OF GENERATIVE AI AND AI-ASSISTED TECHNOLOGIES IN THE WRITING PROCESS

During the preparation of this work, the authors used ChatGPT and DeepSeek to check for grammar errors and typos and improve the clarity of the writing. After using this service, the authors reviewed and edited the content as needed and take full responsibility for the content of the publication.

SUPPLEMENTAL INFORMATION

Supplemental information can be found online at https://doi.org/10.1016/j.patter.2026.101617.

Received: July 10, 2025
Revised: October 17, 2025
Accepted: June 25, 2026

REFERENCES

1. Ono, D., Wang, H., Hung, C.J., Wang, H.-t., Kon, N., Yamanaka, A., Li, Y., and Sugiyama, T. (2023). Network-driven intracellular cAMP coordinates circadian rhythm in the suprachiasmatic nucleus. Sci. Adv. *9*, eabq7032.
2. Enoki, R., Kuroda, S., Ono, D., Hasan, M.T., Ueda, T., Honma, S., and Honma, K.-i. (2012). Topological specificity and hierarchical network of the circadian calcium rhythm in the suprachiasmatic nucleus. Proc. Natl. Acad. Sci. USA *109*, 21498–21503.
3. Pauls, S.D., Honma, K.-I., Honma, S., and Silver, R. (2016). Deconstructing circadian rhythmicity with models and manipulations. Trends Neurosci. *39*, 405–419.
4. Hastings, M.H., Maywood, E.S., and Brancaccio, M. (2018). Generation of circadian rhythms in the suprachiasmatic nucleus. Nat. Rev. Neurosci. *19*, 453–469.
5. Yan, L., Karatsoreos, I., LeSauter, J., Welsh, D., Kay, S., Foley, D., and Silver, R. (2007). Exploring Spatiotemporal Organization of SCN Circuits (Cold Spring Harbor Laboratory Press), pp. 527–541.
6. Brodskiy, P.A., and Zartman, J.J. (2018). Calcium as a signal integrator in developing epithelial tissues. Phys. Biol. *15*, 051001.
7. Brancaccio, M., Maywood, E.S., Chesham, J.E., Loudon, A.S.I., and Hastings, M.H. (2013). A Gq-Ca^{2+} axis controls circuit-level encoding of circadian time in the suprachiasmatic nucleus. Neuron *78*, 714–728.
8. Noguchi, T., Leise, T.L., Kingsbury, N.J., Diemer, T., Wang, L.L., Henson, M.A., and Welsh, D.K. (2017). Calcium circadian rhythmicity in the suprachiasmatic nucleus: cell autonomy and network modulation. eNeuro *4*, 160–177.
9. Enoki, R., Oda, Y., Mieda, M., Ono, D., Honma, S., and Honma, K.-i. (2017). Synchronous circadian voltage rhythms with asynchronous calcium rhythms in the suprachiasmatic nucleus. Proc. Natl. Acad. Sci. USA *114*, E2476–E2485.
10. Wang, Z., Yu, J., Zhai, M., Wang, Z., Sheng, K., Zhu, Y., Wang, T., Liu, M., Wang, L., Yan, M., et al. (2024). System-level time computation and representation in the suprachiasmatic nucleus revealed by large-scale calcium imaging and machine learning. Cell Res. *34*, 493–503.
11. Wen, S., Ma, D., Zhao, M., Xie, L., Wu, Q., Gou, L., Zhu, C., Fan, Y., Wang, H., and Yan, J. (2020). Spatiotemporal single-cell analysis of gene expression in the mouse suprachiasmatic nucleus. Nat. Neurosci. *23*, 456–467.
12. Myung, J., Hong, S., Hatanaka, F., Nakajima, Y., De Schutter, E., and Takumi, T. (2012). Period coding of Bmal1 oscillators in the suprachiasmatic nucleus. J. Neurosci. *32*, 8900–8918.
13. Foley, N.C., Tong, T.Y., Foley, D., LeSauter, J., Welsh, D.K., and Silver, R. (2011). Characterization of orderly spatiotemporal patterns of clock gene activation in mammalian suprachiasmatic nucleus. Eur. J. Neurosci. *33*, 1851–1865.
14. Evans, J.A., Leise, T.L., Castanon-Cervantes, O., and Davidson, A.J. (2011). Intrinsic regulation of spatiotemporal organization within the suprachiasmatic nucleus. PLoS One *6*, e15869.
15. Pauls, S., Foley, N.C., Foley, D.K., LeSauter, J., Hastings, M.H., Maywood, E.S., and Silver, R. (2014). Differential contributions of intra-cellular and inter-cellular mechanisms to the spatial and temporal architecture of the suprachiasmatic nucleus circadian circuitry in wild-type, cryptochrome-null and vasoactive intestinal peptide receptor 2-null mutant mice. Eur. J. Neurosci. *40*, 2528–2540.
16. Pennartz, C.M., De Jeu, M.T., Geurtsen, A.M., Sluiter, A.A., and Hermes, M.L. (1998). Electrophysiological and morphological heterogeneity of neurons in slices of rat suprachiasmatic nucleus. J. Physiol. 775–793 506 (Pt 3).
17. Agostinelli, F., Ceglia, N., Shahbaba, B., Sassone-Corsi, P., and Baldi, P. (2016). What time is it? Deep learning approaches for circadian rhythms. Bioinformatics *32*. i8–i17.
18. Anafi, R.C., Lee, Y., Sato, T.K., Venkataraman, A., Ramanathan, C., Kavakli, I.H., Hughes, M.E., Baggs, J.E., Growe, J., Liu, A.C., et al. (2014). Machine learning helps identify CHRONO as a circadian clock component. PLoS Biol. *12*, e1001840.
19. Czeisler, M.É., Shan, Y., Schalek, R., Berger, D.R., Suissa-Peleg, A., Takahashi, J.S., and Lichtman, J.W. (2024). Extensive soma-soma plate-like contact sites (ephapses) connect suprachiasmatic nucleus neurons. J. Comp. Neurol. *532*, e25624.
20. Hughey, J.J. (2017). Machine learning identifies a compact gene set for monitoring the circadian clock in human blood. Genome Med. *9*. 1–11.
21. Hutson, M. (2022). Taught to the test. Science *376*, 570–573.
22. Yamaguchi, S., Isejima, H., Matsuo, T., Okura, R., Yagita, K., Kobayashi, M., and Okamura, H. (2003). Synchronization of cellular clocks in the suprachiasmatic nucleus. Science *302*, 1408–1412.
23. Maywood, E.S., Drynan, L., Chesham, J.E., Edwards, M.D., Dardente, H., Fustin, J.-M., Hazlerigg, D.G., O'Neill, J.S., Codner, G.F., Smyllie, N.J., et al. (2013). Analysis of core circadian feedback loop in suprachiasmatic nucleus of mCry1-luc transgenic reporter mouse. Proc. Natl. Acad. Sci. USA *110*, 9547–9552.
24. Schaap, J., Albus, H., VanderLeest, H.T., Eilers, P.H.C., Détári, L., and Meijer, J.H. (2003). Heterogeneity of rhythmic suprachiasmatic nucleus neurons: Implications for circadian waveform and photoperiodic encoding. Proc. Natl. Acad. Sci. USA *100*, 15994–15999.
25. Syakur, M.A., Khotimah, B.K., Rochman, E., and Satoto, B.D. (2018). Integration K-Means Clustering Method and Elbow Method for Identification of the Best Customer Profile Cluster (IOP Publishing), pp. 012017.
26. Schwarz, G. (1978). Estimating the dimension of a model. Ann. Stat. 461–464.
27. Huang, Z., and Ng, M.K. (1999). A fuzzy k-modes algorithm for clustering categorical data. IEEE Trans. Fuzzy Syst. *7*, 446–452.
28. de la Iglesia, H.O., Meyer, J., and Schwartz, W.J. (2003). Lateralization of circadian pacemaker output: activation of left-and right-sided luteinizing hormone-releasing hormone neurons involves a neural rather than a humoral pathway. J. Neurosci. *23*, 7412–7414.
29. Yan, L., Foley, N.C., Bobula, J.M., Kriegsfeld, L.J., and Silver, R. (2005). Two antiphase oscillations occur in each suprachiasmatic nucleus of behaviorally split hamsters. J. Neurosci. *25*, 9017–9026.
30. de la Iglesia, H.O., Meyer, J., Carpino, A., Jr., and Schwartz, W.J. (2000). Antiphase oscillation of the left and right suprachiasmatic nuclei. Science *290*, 799–801.
31. Ohta, H., Yamazaki, S., and McMahon, D.G. (2005). Constant light desynchronizes mammalian clock neurons. Nat. Neurosci. *8*, 267–269.
32. Pickard, G.E., and Turek, F.W. (1982). Splitting of the circadian rhythm of activity is abolished by unilateral lesions of the suprachiasmatic nuclei. Science *215*, 1119–1121.

33. Davis, F.C., and Gorski, R.A. (1984). Unilateral lesions of the hamster suprachiasmatic nuclei: evidence for redundant control of circadian rhythms. J. Comp. Physiol. *154*, 221–232.

34. de la Iglesia, H.O., Cambras, T., Schwartz, W.J., and Díez-Noguera, A. (2004). Forced Desynchronization of Dual Circadian Oscillators within the Rat Suprachiasmatic Nucleus. Curr. Biol. *14*, 796–800.

35. van den Pol, A.N., Finkbeiner, S.M., and Cornell-Bell, A.H. (1992). Calcium excitability and oscillations in suprachiasmatic nucleus neurons and glia in vitro. J. Neurosci. *12*, 2648–2664.

36. Hong, J.H., Min, C.H., Jeong, B., Kojiya, T., Morioka, E., Nagai, T., Ikeda, M., and Lee, K.J. (2010). Intracellular Calcium Spikes in Rat Suprachiasmatic Nucleus Neurons Induced by BAPTA-Based Calcium Dyes. PLoS One *5*, e9634.

37. El Cheikh Hussein, L., Fontanaud, P., Mollard, P., and Bonnefont, X. (2022). Nested calcium dynamics support daily cell unity and diversity in the suprachiasmatic nuclei of free-behaving mice. PNAS Nexus *1*, pgac112.

38. Kononenko, N.I., and Dudek, F.E. (2004). Mechanism of Irregular Firing of Suprachiasmatic Nucleus Neurons in Rat Hypothalamic Slices. J. Neurophysiol. *91*, 267–273.

39. Mazuski, C., Abel, J.H., Chen, S.P., Hermanstyne, T.O., Jones, J.R., Simon, T., Doyle, F.J., III, and Herzog, E.D. (2018). Entrainment of Circadian Rhythms Depends on Firing Rates and Neuropeptide Release of VIP SCN Neurons. Neuron *99*, 555–563.e5.

40. Stratton, P., and Wiles, J. (2008). Comparing Kurtosis Score to Traditional Statistical Metrics for Characterizing the Structure in Neural Ensemble Activity. In Dynamic Brain - from Neural Spikes to Behaviors: 12th International Summer School on Neural Networks, Erice, Italy, December 5-12, 2007, Revised Lectures, M. Marinaro, S. Scarpetta, and Y. Yamaguchi, eds. (Springer Berlin Heidelberg), pp. 115–122.

41. Bhumbra, G.S., Inyushkin, A.N., Saeb-Parsy, K., Hon, A., and Dyball, R.E.J. (2005). Rhythmic changes in spike coding in the rat suprachiasmatic nucleus. J. Physiol. *563*, 291–307.

42. Pennartz, C.M.A., de Jeu, M.T.G., Bos, N.P.A., Schaap, J., and Geurtsen, A.M.S. (2002). Diurnal modulation of pacemaker potentials and calcium current in the mammalian circadian clock. Nature *416*, 286–290.

43. Belle, M.D.C., Diekman, C.O., Forger, D.B., and Piggins, H.D. (2009). Daily Electrical Silencing in the Mammalian Circadian Clock. Science *326*, 281–284.

44. Diekman, C.O., Belle, M.D.C., Irwin, R.P., Allen, C.N., Piggins, H.D., and Forger, D.B. (2013). Causes and Consequences of Hyperexcitation in Central Clock Neurons. PLoS Comput. Biol. *9*, e1003196.

45. Ginsberg, A.G., and Booth, V. (2023). A Mean-Field Firing-Rate Model for the Suprachiasmatic Nucleus. SIAM J. Appl. Dyn. Syst. *22*, 90–128.

46. Wegner, S., Belle, M.D.C., Chang, P.-S., Hughes, A.T.L., Conibear, A.E., Muir, C., Samuels, R.E., and Piggins, H.D. (2024). Loss of neuropeptide signalling alters temporal expression of mouse suprachiasmatic neuronal state and excitability. Eur. J. Neurosci. *60*, 6617–6633.

47. Ocklenburg, S., Peterburs, J., and Mundorf, A. (2022). Hemispheric asymmetries in the amygdala: A comparative primer. Prog. Neurobiol. *214*, 102283.

48. Martin, S.J., Shires, K.L., and da Silva, B.M. (2019). Hippocampal Lateralization and Synaptic Plasticity in the Intact Rat: No Left-Right Asymmetry in Electrically Induced CA3-CA1 Long-Term Potentiation. Neuroscience *397*, 147–158.

49. Baban, W.M. (2019). Right/Left Hemisphere Lateralization: Correlation Between Individual Differences in Subjective Wellbeing, Happiness, Life Satisfaction, Success, Personality and Thinking Styles. In Undergraduate Research Symposium. 9. https://irl.umsl.edu/urs/9

50. Schwartz, W.J., and Zimmerman, P. (1991). Lesions of the suprachiasmatic nucleus disrupt circadian locomotor rhythms in the mouse. Physiol. Behav. *49*, 1283–1287.

51. Silva, C.-C., Benítez, D.P., Flores, A., Cortés, G.D., Vieyra, E., Juárez-Tapia, C.R., Romero-Reyes, J., and Domínguez, R. (2023). Unilateral lesion of the suprachiasmatic nucleus impairs estradiol feedback, follicular development, estrous cycle and ovulation. Reproduction *166*, 459–471.

52. Nagano, M., Adachi, A., Nakahama, K.-i., Nakamura, T., Tamada, M., Meyer-Bernstein, E., Sehgal, A., and Shigeyoshi, Y. (2003). An Abrupt Shift in the Day/Night Cycle Causes Desynchrony in the Mammalian Circadian Center. J. Neurosci. *23*, 6141–6151.

53. Yan, L., Foley, N.C., Bobula, J.M., Kriegsfeld, L.J., and Silver, R. (2005). Two Antiphase Oscillations Occur in Each Suprachiasmatic Nucleus of Behaviorally Split Hamsters. J. Neurosci. *25*, 9017–9026.

54. Lee, M.L., Swanson, B.E., and de la Iglesia, H.O. (2009). Circadian Timing of REM Sleep Is Coupled to an Oscillator within the Dorsomedial Suprachiasmatic Nucleus. Curr. Biol. *19*, 848–852.

55. Schwartz, M.D., Wotus, C., Liu, T., Friesen, W.O., Borjigin, J., Oda, G.A., and de la Iglesia, H.O. (2009). Dissociation of circadian and light inhibition of melatonin release through forced desynchronization in the rat. Proc. Natl. Acad. Sci. USA *106*, 17540–17545.

56. Kim, H., Min, C., Jeong, B., and Lee, K.J. (2022). Deciphering clock cell network morphology within the biological master clock, suprachiasmatic nucleus: From the perspective of circadian wave dynamics. PLoS Comput. Biol. *18*, e1010213.

57. Rogers, L.J., and Deng, C. (1999). Light experience and lateralization of the two visual pathways in the chick. Behav. Brain Res. *98*, 277–287.

58. Larsson, M. (2013). The optic chiasm: a turning point in the evolution of eye/hand coordination. Front. Zool. *10*, 41.

59. Kanno, K., Shima, S., Ishida, Y., and Yamanouchi, K. (2008). Ipsilateral and contralateral serotonergic projections from dorsal and median raphe nuclei to the forebrain in rats: immunofluorescence quantitative analysis. Neurosci. Res. *61*, 207–218.

60. DeCoursey, P.J. (1960). Phase Control of Activity in a Rodent (Cold Spring Harbor Laboratory Press), pp. 49–55.

61. Daan, S., and Pittendrigh, C.S. (1976). A functional analysis of circadian pacemakers in nocturnal rodents. II. The variability of phase response curves. J. Comp. Physiol. *106*, 253–266.

62. Kim, J.K., Forger, D.B., Marconi, M., Wood, D., Doran, A., Wager, T., Chang, C., and Walton, K.M. (2013). Modeling and Validating Chronic Pharmacological Manipulation of Circadian Rhythms. CPT-Pharmacomet. Syst. *2*, 57.

63. Kim, D.W., Chang, C., Chen, X., Doran, A.C., Gaudreault, F., Wager, T., DeMarco, G.J., and Kim, J.K. (2019). Systems approach reveals photosensitivity and PER2 level as determinants of clock-modulator efficacy. Mol. Syst. Biol. *15*, e8838.

64. Ocklenburg, S., and Guo, Z.V. (2024). Cross-hemispheric communication: Insights on lateralized brain functions. Neuron *112*, 1222–1234.

65. Chao, H.-T., Chen, H., Samaco, R.C., Xue, M., Chahrour, M., Yoo, J., Neul, J.L., Gong, S., Lu, H.-C., Heintz, N., et al. (2010). Dysfunction in GABA signalling mediates autism-like stereotypies and Rett syndrome phenotypes. Nature *468*, 263–269.

66. Kim, Y.S., Anderson, M., Park, K., Zheng, Q., Agarwal, A., Gong, C., Saijilafu, Young, L., He, S., LaVinka, P.C., et al. (2016). Coupled activation of primary sensory neurons contributes to chronic pain. Neuron *91*, 1085–1096.

67. Madisen, L., Garner, A.R., Shimaoka, D., Chuong, A.S., Klapoetke, N.C., Li, L., Van Der Bourg, A., Niino, Y., Egolf, L., Monetti, C., et al. (2015). Transgenic mice for intersectional targeting of neural sensors and effectors with high specificity and performance. Neuron *85*, 942–958.

68. Zhai, M., Yu, J., Hu, Y., Yu, H., Xie, B., Yu, Y., Li, D., Wang, A., and Cheng, H. (2024). Dual-objective two-photon microscope for volumetric imaging of dense scattering biological samples by bidirectional excitation and collection. Photonics Res. *12*, 1351–1361.

69. Pei, J., Deng, L., Song, S., Zhao, M., Zhang, Y., Wu, S., Wang, G., Zou, Z., Wu, Z., He, W., et al. (2019). Towards artificial general intelligence with hybrid Tianjic chip architecture. Nature *572*, 106–111.

70. Chen, G., Scherr, F., and Maass, W. (2022). A data-based large-scale model for primary visual cortex enables brain-like robust and versatile visual processing. Sci. Adv. *8*, eabq7592.

71. Yin, B., Corradi, F., and Bohté, S.M. (2021). Accurate and efficient time-domain classification with adaptive spiking recurrent neural networks. Nat. Mach. Intell. *3*, 905–913.

72. Fang, W., Chen, Y., Ding, J., Yu, Z., Masquelier, T., Chen, D., Huang, L., Zhou, H., Li, G., and Tian, Y. (2023). Spikingjelly: An open-source machine learning infrastructure platform for spike-based intelligence. Sci. Adv. *9*, eadi1480.

73. Neftci, E.O., Mostafa, H., and Zenke, F. (2019). Surrogate gradient learning in spiking neural networks: Bringing the power of gradient-based optimization to spiking neural networks. IEEE Signal Process. Mag. *36*, 51–63.

74. Kingma, D.P., and Ba, J. (2015). Adam: A method for stochastic optimization. In International Conference on Learning Representations (ICLR), pp. 1–15.

75. Torchiano, M. (2016). Effsize - a package for efficient effect size computation. Zenodo. https://doi.org/10.5281/zenodo.196082.

76. Cohen, J. (2013). Statistical Power Analysis for the Behavioral Sciences (Routledge).

77. Cohen, J. (1992). Quantitative methods in psychology: A power primer. Psychol. Bull. *112*, 1155–1159.

78. Barandas, M., Folgado, D., Fernandes, L., Santos, S., Abreu, M., Bota, P., Liu, H., Schultz, T., and Gamboa, H. (2020). TSFEL: Time series feature extraction library. SoftwareX *11*, 100456.

79. McHugh, M.L. (2012). Interrater reliability: the kappa statistic. Biochem. Med. *22*, 276–282.

80. He, K., Zhang, X., Ren, S., and Sun, J. (2016). Deep residual learning for image recognition. Proc. IEEE Comput. Soc. Conf. Comput. Vis. Pattern Recognit. 770–778.

81. Wang, Z., Yu, J., and Zhang, Z. (2025). 2D-t calcium imaging dataset of suprachiasmatic nucleus. Zenodo. https://doi.org/10.5281/zenodo.15817326

82. Zhang, Z. (2026). Code for "Interpretable machine learning reveals hemispheric asymmetry of state switching in the suprachiasmatic nucleus". Zenodo. https://doi.org/10.5281/zenodo.20637473